Cenozoic kinematics of the Wenchuan-Maoxian fault implies crustal stacking rather than channel flow extrusion at the Tibetan plateau eastern margin (Longmen Shan)

Chenglong Ge, Philippe Hervé Leloup, Yong Zheng, Stéphane Scaillet, Laura Airaghi, Florian Duval, Jinjiang Zhang, Haibing Li

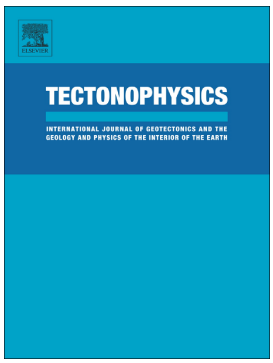

Cenozoic kinematics of the Wenchuan-Maoxian fault implies crustal stacking rather than channel flow extrusion at the Tibetan plateau eastern margin (Longmen Shan)

G.E. Chenglong, Philippe Hervé Leloup, Yong Zheng, Stéphane Scaillet, Laura Airaghi, Florian Duval, Jinjiang Zhang, Haibing Li

PII: S0040-1951(23)00114-2

DOI: https://doi.org/10.1016/j.tecto.2023.229816

Reference: TECTO 229816

To appear in: *Tectonophysics*

Received date: 27 December 2022

Revised date: 3 March 2023

Accepted date: 10 March 2023

Please cite this article as: G.E. Chenglong, P.H. Leloup, Y. Zheng, et al., Cenozoic kinematics of the Wenchuan-Maoxian fault implies crustal stacking rather than channel flow extrusion at the Tibetan plateau eastern margin (Longmen Shan), *Tectonophysics* (2023), https://doi.org/10.1016/j.tecto.2023.229816

Cenozoic kinematics of the Wenchuan-Maoxian fault implies crustal stacking rather than channel flow extrusion at the Tibetan plateau eastern margin (Longmen Shan).

Chenglong GE[1,2,3], Philippe Hervé Leloup[3], Yong Zheng[1], Stéphane Scaillet[4], Laura Airaghi[4], Florian Duval[4], Jinjiang Zhang[2], Haibing Li[1]*

1 Key Laboratory of Deep-Earth Dynamics of Ministry of Natural Resources, Institute of Geology, Chinese Academy of Geological Sciences, Beijing 100037, China
2 School of Earth and Space Sciences, Peking University, Beijing, China
3 Laboratoire de Géologie de Lyon, Terre, Planètes, Environnement, Lyon, Université Lyon 1; ENS de Lyon; CNRS UMR 5276, 2 rue Raphaël Dubois, 69622, Villeurbanne, France
4 Université Orléans, CNRS, BRGM, Institut des Sciences de la Terre d'Orléans (ISTO), UMR 7327, F-45071, Orléans, France

** Corresponding author*

Keywords:
Longmen Shan, brittle/ductile faulting, fault gouge dating, Petro-geochronology, in-situ/step-heating $^{40}Ar/^{39}Ar$ dating, mountain building

Abstract

The Longmen Shan, eastern and steepest margin of the Tibetan plateau, is often seen as the archetype example of an orogenic system built by crustal channel flow extrusion since the Miocene. This model is controversial as other studies propose an accretionary prism mechanism. A key difference between these models resides in the kinematics proposed for the Wenchuan - Maoxian (WM) fault zone, a major tectonic structure of the Longmen Shan. We constrain the Cenozoic kinematics of the WM fault zone by combining structural observations, fault gouge K/Ar dating and $^{40}Ar/^{39}Ar$ dating of syn-kinematic white mica. Normal / right lateral ductile deformation occurred at 28.0 ± 0.9 Ma while top-to-the-east reverse deformation at 15.4 ± 0.2 Ma. K-Ar ages of authigenic illite from two fault gouges show that brittle right-lateral / reverse deformation was active at 6.9 ± 2.9 Ma. These ages are consistent with the relative vertical motions across the fault zone deduced from thermochronology. Three deformation phases can be identified: right-lateral / normal in the Middle Oligocene (~30 - 25 Ma), reverse in the middle Miocene (25-15 Ma), and right-lateral / reverse since the upper Miocene (since ~6 Ma). The WM fault zone never experienced pure normal motion, and only shortening since the Oligocene, in contrast to predictions of lower crustal channel-flow extrusion models. These results are in favor of a crustal accretionary prism model for the Cenozoic building of the eastern Tibetan plateau.

1 Introduction

The Tibetan plateau with an average elevation >5000 m a.s.l., and a 65-80 km-thick crust, is the largest high plateau on earth. Geological and geophysical studies suggest it has a complex structure largely shaped by the India / Eurasia collision since ~55 Ma (e.g.: Tapponnier et al., 2001; Yin and Harrison, 2000). Various models corresponding to contrasted views of the continental lithosphere rheology have been proposed to explain the Cenozoic formation and evolution of the Tibetan plateau.

Lateral extrusion of partially molten crustal material outward from below the Tibetan plateau has been proposed for the building of the Himalaya and Eastern Tibet structure and topography. Such mechanism would be strongly coupled with high erosion focussed on the ranges slope and would explain extrusion of a piece of crust between parallel and coeval thrust at the base and normal fault at the top. Central to this model is the geophysical (seismic, magnetotelluric) observation of widespread Low Velocity Zones (LVZ) within the crust interpreted as diagnostic of present-day partial melting and thus extremely weak rheology (e.g., Nelson et al., 1996; Klemperer, 2006), that would decouple deformation in the upper crust from that in the lower crust / upper mantle.

In the Himalaya, channel flow has been suggested to explain lower Miocene extrusion of partially molten gneisses of the Greater Himalayan Sequence between the Main Central Thrust at the base of the range and the South Tibet Detachment at the top (e.g.; Beaumont et al., 2001; Jamieson et al., 2004; Searle and Szulc, 2005). This popular model may be questioned because the partial melting, the Main Central Thrust and the South Tibet Detachment are not exactly synchronous (e.g., Leloup et al., 2015). Some still favour an accretionary prism model where the structure and topography of the Himalaya result from crustal stacking in an accretionary prism (e.g., Bollinger at al., 2006; Kohn et al., 2008).

In any case, motion on the South Tibet Detachment, and thus potential channel flow toward the south, ended between 13 and 11 Ma ago (e.g., Leloup et al., 2010). Since ~15 Ma (middle Miocene) crustal flow would have veered toward the east inducing E-W extension in Central Tibet and outward migration of the eastern Tibet topography (e.g., Klemperer, 2006; Adams and Hodges, 2022). That second phase of channel flow would have created the world's steepest topographic continental slope in the Longmen Shan (LMS) towering nearly 5000 m above the Sichuan basin (Fig. 1c). Lower crustal material expelled from below Tibet would inflate when buttressing against the rigid South China craton (e.g., Royden et al., 1997; Clark and Royden, 2000), generating coeval reverse fault at the bottom and normal fault at the top (Fig. 2b) (e.g., Clark et al., 2005a, b; Royden et al., 2008; Burchfiel et al., 2008). This makes of the LMS an archetype example of an orogenic system built by crustal channel flow extrusion since the Miocene. But others rather advocate thickening through crustal stacking on reverse faults where deformation in the upper crust is strongly coupled with that in the lower crust / upper mantle (e.g., Hubbard and Shaw, 2009; Hubbard et al., 2010; Li et al., 2010; Tian et al., 2013; Wu et al., 2014; Lu et al., 2016) (Fig. 2a). One of the key points to distinguish between these models is the kinematics of the Wenchuan-Maoxian (WM) fault zone located in the internal part of

the belt: in the lower crustal flow extrusion model the fault should show a normal component of motion coeval with thrusting at the front of the range (Fig. 2b).

Kinematics of the WM fault zone is however still poorly documented especially for the Miocene, at a time when lower crustal flow is thought to be dominant (e.g., Clark et al., 2005a). In this work we combine structural geology with illite K/Ar dating on fault gouges and *in situ* and step-heating $^{40}Ar/^{39}Ar$ dating of mica in greenschist-facies rocks deformed along the fault system to constrain the kinematics of the WM fault zone since ~30 Ma, and thus to discuss the Longmen Shan building mechanism(s).

2 Geological background.

2.1 The Longmen Shan belt.

The Longmen Shan separates the Songpan-Ganze block (Tibetan plateau) in the west from the Sichuan Basin in the east and is straddled from west to east by three major sub-parallel fault zones: Wenchuan-Maoxian (WM), Yingxiu-Beichuan, and Guanxian-Anxian (Fig. 1b) (e.g., SBGMR 1991). Surface geology and geophysical studies suggest that the faults are NW-dipping, listric and that they merge into a detachment at depth of ~20-30 km (Feng et al., 2010; Hubbard and Shaw, 2009). In the Central Longmen Shan, three basement complexes (Pengguan (PG), Mutuo (MT) and Xuelongbao (XLB)) are composed of Neoproterozoic meta-granites unconformably overlain by a Neoproterozoic meta-sedimentary cover (Sinian). They are bounded by the WM and Yingxiu Beichuan faults and structured in NW dipping slices (Fig. 1b, c) (Xu et al., 2009; Yan et al., 2011; Airaghi et al., 2017; Xue et al., 2021).

A major phase of top to the SE thrusting is evidenced by penetrative cleavage and stretching lineation in the metasediments in the Wenchuan area, and by nappe emplacement over the strongly folded Late Triassic sequences in the western Sichuan foreland basin (Burchfiel et al., 1995; Worley and Wilson, 1996; Mattauer, 1992; Yan et al., 2011). During that phase the metasedimentary rocks northwest of the Pengguan complex reached amphibolite-facies metamorphic conditions at ~11 ± 2 kbar and ~620 °C (Dirks et al., 1994; Airaghi et al., 2019). These conditions were reached at ca. 224–180 Ma (Upper Triassic – Lower Jurassic) (Yan et al., 2011; Airaghi et al., 2018b; 2019; Xue et al., 2021). The Pengguan complex experienced further exhumation at ca. 140 – 120 Ma (Lower Cretaceous) (Arne et al., 1997; Airaghi et al., 2018a).

In the Longmen Shan, localized crustal shortening models are supported by observations of east-verging Cenozoic thrust faults in the foreland (e.g., Hubbard and Shaw, 2009; Hubbard et al., 2010) (Fig. 2a). Channel flow models are based instead on the lack of significant shortening across the belt both at short time scale according to GPS measurements (e.g., Zhang et al., 2004), and at longer time scale because of the absence of significant flexural basin of Cenozoic age (e.g., Burchfiel et al., 1995). Geophysical evidence for low velocity layers in the lower crust of Tibet suggest that the lower crust is soft enough for channel flow to occur (e.g., Yao et al., 2006, 2008; Li et al., 2009). In this view, the flow of soft lower crust would have propagated eastward during the Miocene (Fig. 2b) (Royden et al., 2008). Activation of the

Guanxian-Anxian and Yingxiu-Beichuan faults at the front of the LMS during the 2008 Mw7.9 Wenchuan earthquake implies that thrusting with a right-lateral component on NE-SW NW dipping faults is a major active mechanism in the Longmen Shan building (e.g., Xu et al., 2009) (Fig. 1b)

2.2 The Wenchuan - Maoxian fault zone.

In the Central Longmen Shan the Wenchuan-Maoxian (WM) fault zone is a ~120 km long, NE-SW striking, NW-dipping fault network that separates Proterozoic basement rocks in the south-east from metamorphosed Paleozoic sediments in the north-west (SBGMR, 1991). The fault zone underwent a polyphase history (e.g., Burchfiel et al., 1995) since the Paleozoic. Raman spectrometry measurements of carbonaceous material (RSCM) suggest the basement rocks never exceeded 360 °C while the Paleozoic sediments that experienced temperature conditions of 450-600 °C (Airaghi et al., 2018a).

Within the WM fault zone, there is evidence for brittle deformation with fault planes, fault gouge and brecciated rocks along the WM fault (Dirks et al., 1994, Burchfiel et al., 1995; Wang et al., 2014; Airaghi, 2017) (Fig. 3a). Slickensides on fault planes are dominantly horizontal but also show pitches up to 30° SW, indicating right lateral / reverse motion for some authors (Burchfiel et al., 1995) or left-lateral for others (Dirks et al., 1994). Yet, other authors suggest pure reverse motion (Wang et al., 2014), or a more complex history with left-lateral then right-lateral motion (Airaghi, 2017). Dog-leg's river deflections and possible shutter ridges suggest that the right-lateral motion is recent and possibly still active (Burchfiel et al., 1995; Densmore et al., 2005). Some late Pleistocene fluvial terraces, dated at ~20–24 ka by radiocarbon and thermoluminescence methods, were uplifted above the Minjiang riverbed by ~20–50 m, suggesting a minimum Quaternary vertical thrust rate of ~0.5–1.1 mm/yr. across the WM fault (Li et al., 2006; Zhou et al., 2006), and a right-lateral rate of 0.8 to 1 mm/yr. (Zhou et al., 2006). However, based on the spatial distribution of the basin-wide denudation rates inferred from cosmogenic dating, Godard et al. (2010) propose that there is no significant recent differential uplift across the WM fault.

Mylonites with steep lineation are found both in the Proterozoic basement east of the brittle WM fault and in metamorphosed Paleozoic sediments in the west (Burchfiel et al., 1995, Airaghi et al., 2019; Xue et al., 2021). S/C shear criteria generally indicate top to the SE (reverse) motion, but top to NW (normal) is observed southeast of the WM fault (Xu et al., 2008; Burchfiel et al., 1995; Xue et al., 2021). ~120 km further south in the Southern Longmen Shan, Cretaceous-Paleogene ductile top to the NW (normal) deformation is found in gneiss west of the WM fault (Tian et al., 2016). However, there are no similar structures in the Central Longmen Shan, possibly because the structural evolution of the southern Longmen Shan is markedly different from than that of the central one (Airaghi et al., 2018a). West of the WM fault, the metamorphism shows a prograde path coeval with thickening with peak metamorphism reached at ~180 Ma, and retrograde evolution lasting until ~120 Ma, prior to activation of the WM fault zone sometime after 100 Ma (Airaghi et al., 2018b, 2019). East of the WM fault, white micas in mylonite showing top to the west (normal)

shear criteria yield an $^{40}Ar/^{39}Ar$ weighted mean age of 26.2 ± 1.0 Ma, while other samples showing similar deformation have disturbed age spectra with apparent ages between 50 and 140 Ma (Xue et al., 2021). These ages are interpreted to reflect episodic normal faulting from Lower Cretaceous to Miocene (Xue et al., 2021).

Low-temperature thermochronology across the fault constrains the vertical motion on the WM fault zone. Shen et al. (2019) estimate that the WM behaved as a reverse fault zone at ~0.6 mm/yr. since 12-15 Ma. Furlong et al. (2021) infer a more complex history with the WM fault behaving as a thrust between ~20 and ~15 Ma, then stopping before resuming at 10-6 Ma with a vertical rate >0.6 mm/yr.

3. Field constraints on the structural evolution of the Wenchuan-Maoxian (WM) fault zone.

3.1. Ductile kinematics.

Our study across the WM fault near Gengda documents a ~3 km wide ductile deformation belt on both sides of the brittle WM fault (Fig. 4a, b). Within this belt, foliations trend N164° to N150° and dip 40°- 85° to the NW (Fig. 4c, d). Within the Paleozoic metamorphosed sediments west of the fault steep cleavage planes are cut by shallower shear planes bearing WSW-ENE trending lineation (Fig. 4c, Fig. 5a, b). These S/C relationships suggest top to the east (reverse) motion. At the microscopic scale shear criteria are sometime ambiguous, but when clear they systematically suggest top the east motion (Fig. 5e). These rocks have White mica + Chlorite + recrystallized Quartz in the shear planes and along the foliation, and Feldspar ± Epidote porphyroclasts, with feldspars deforming brittlely (Fig. 5c).

Within the Proterozoic basement of the Pengguan massif the lineation trend to the NNW (Fig. 4d). Shear criteria are not clear in the field but in thin section they suggest top to the NW (right-lateral / normal) motion (Fig. 5f). These rocks show White mica + Chlorite + recrystallized Quartz in the shear planes and along the foliation, and Feldspar ± Epidote ± Amphibole porphyroclasts in the matrix. Some of the feldspar show evidence for ductile deformation (Fig. 5f) suggesting higher deformation temperature of deformation than in the schists west of the fault. However, other factors as the deformation rate can influence the mechanical behaviour of K-feldspar during deformation. Xue et al. (2021) also report top to the NW (normal) deformation along the boundary of the Pengguan east of the WM fault. The ductile deformation zone thus appears to result from two distinct deformations: top to the east (reverse) in the Paleozoic metamorphic rocks and top to the NW (normal / right lateral) at the margin of the Pengguan. No outcrop with both deformations could be found, precluding the observation of any crosscutting relationship.

3.2. Brittle kinematics.

As evoked above, some lines of evidence point to a recent dominant strike-slip motion on the brittle WM fault, with presumably a right-lateral / reverse motion (e.g., Burchfiel et al., 1995). Our own observations document brittle deformation zones at several sites along the WM fault (Fig. 3a). At site MW19-11, near Gengda, gneiss,

micaschists and calcschists are affected by ductile reverse / left-lateral deformation compatible to that seen further north, east of the brittle fault. These structures are overprinted by brecciation along faults trending ~N30° parallel to the WM fault (Fig. 3a). At site MW19-81 granites are brecciated and bounded by a clear fault plane trending N25° 61°W bearing striation with a pitch of 64°S (Fig. 3a). At site MW19-79 the WM fault crops out as a ~50 m thick brittle fault zone, with soft, deep dark and strongly foliated gouges, framing a grey fault breccia zone with a less organized structure (Fig. 6a, d). The fault planes strike between N38° and N65°, dip steeply to the NW and show slickensides with pitches of ~10° to 40° toward the SW (Fig. 6c). An oriented sample taken from the black fault gouge against the NW fault plane (Fig. 6b) shows angular quartz clasts surrounded by a black clay-rich matrix whose foliation orientation with respect to that of the fault plane (shear plane) indicate right-lateral shear (Fig. 6e). Similar structures and Riedel shear elements can be also seen at the microscopic scale (Fig. 6f. g. h). Pitch values of striations imply a component of reverse motion.

3.3. Quantitative offset estimates.

One important aspect of the WM fault zone kinematics is that it can be constrained by bedrock geology (reflecting long-term changes in metamorphic grade) and morphology (manifesting shorter-term changes in active topography).

Total exhumation appears more important SE of the fault zone, where basement rocks are more widely exposed in the Pengguan complex (4969 m), than in the NW where such rocks only outcrop in the Xuelongbao (5313 m) and Mutuo (3455 m) ranges (Fig. 3a). This could imply that the WM fault zone is a normal fault (e.g., Royden et al., 2008). However, the metasediments NW of the fault experienced higher temperature metamorphism (450-600 °C) during the Triassic than those from the Pengguan range (≤360 °C) (Airaghi et al., 2018a). This rather suggests an overall reverse motion since the Triassic. From a limited thermochronology data set Godard et al., (2009) concluded that there was no significant vertical motion across the WM fault since ~11 Ma. However, from a much larger dataset Furlong et al. (2021) recently estimated ~2 km more Cenozoic exhumation of the Xuelongbao than the Pengguan, implying a reverse component of motion. Taking the base of the Sinian sedimentary cover as a piercing point across the fault suggests an apparent right-lateral offset of ~27 km (NE of both the Pengguan and Mutuo complexes; Fig. 3a and S1-1). Maps of river channel steepness do not show a strong contrast across the WM fault, suggesting that the fault has no dip-slip motion at present (Kirby and Ouimet, 2011).

Geologic markers as well as geomorphologic offset patterns such as deflected river network (e.g., Gaudemer et al., 1989) provide insight into mid- to short-term horizontal motion accumulated along the WM fault. Using the river network may not be straightforward because rivers are not passive markers. However, in the case of deeply incised rivers, lateral motion of the river-bed is greatly limited, and those rivers may be considered as clear piercing points. This is the case for the lower reach of the major Minjiang River (Fig. 3a) which is one of the only two rivers flowing across the Pengguan range in deep gorges (Fig. 1c). Upstream, the Minjiang river is

strongly deflected toward the NE along the WM fault for ~59 km until Maoxian town, where it suddenly veers ~90° to flow out of the Tibetan Plateau (Fig. 3a). Taken at face value, this piercing point would suggest a ~59 km right-lateral offset since river incision. However, such offset does not realign the Zagunao river, the only other major river draining Tibet in this area (Fig. 3a), with any downstream counterpart. Furthermore, the implied river offset is more than twice as large than the geological one when it should be equal or smaller as it is necessarily younger. Taking the Zagunao river as the upper reach of the Minjiang prior to the onset of the WM fault instead yields a ~25 km offset (Fig. 3b). That offset also aligns the upstream Caoba river with the downstream Yuzixi river that is the other river flowing across the Pengguan range (Fig. 3). This offset is consistent with that seen in the geology (~27 km) (Fig. 3a and S1-1b). The ~25 km offset does not realign the upper reach of the Minjiang with any downstream counterpart, but with the Qianjiang river. However, these two rivers are now disconnected as they are separated by the Pengguan range (Fig. 3b). This could be due to the fact that uplift of the Pengguan may have been too fast for the Qianjiang to entrench, disconnecting it from the upstream river network while the Minjiang and the Yuzixi rivers eroded fast enough to cross the Pengguan. This interpretation is consistent with the detailed geometry of the river network by also matching thirteen valleys across the fault (Figs S1-1 and S1-2). Accordingly, the flow direction would have been inverted for five ~10 km-long river stretches (8' to 13') by the fast uplift of the Pengguan. While tentative, such reconstruction provides the simplest scenario for the recent river network evolution, in particular by accounting for the fact that the WM fault, for which there is clear evidence of strike-slip motion, did necessarily offset the river network. Integration of the river offset pattern with the finite-strain structural-metamorphic record is discussed further in Sections 5.1 and 5.2 based on temporal constraints described below.

4 Temporal constraints

4.1 K-Ar dating of fault gouge

Dating of fault gouge can constrain the timing of brittle deformation (Vrolijk et al., 2018). Natural fault gouge usually contains a mixture of two illite polytypes, $2M_1$ and $1M_d$. Only $1M_d$ polytype is considered to form simultaneously with faulting and usually has a size < 2 μm, in contrast to the larger $2M_1$ polytype inherited from wall-rock material. The age of the $1M_d$ polytype would thus tend to be closer to that of deformation while that of the $2M_1$ will be inherited (Haines and van der Pluijm, 2008). Considering the fine grain size of illite mineral, the K-Ar method is more appropriate than the $^{40}Ar/^{39}Ar$ because of recoil effects during neutron irradiation (Clauer, 2013). We present results from two fault gouge samples taken at site MW19-79 near both fault planes framing the gouge zone (Fig. 6d, see detail in table 1). The samples were disaggregated and separated via gravitational floating and centrifugation to isolate clay fraction with four sizes, 1-2, 0.5-1, 0.25-0.5 and <0.25 μm, which were then characterized using X-ray diffraction and analysed with PROFEX software to quantify illite polytypes (Bergmann et al., 1998) (Fig. S2-1, S2-2; table S2-1). Each size fraction was dated using the K-Ar method as described by Zheng et al., (2014),

and ages are plotted against the percentage of $2M_1$ polytype (Fig. 7, Tables S2-2, S2-3). Details on the analytical procedure are found in Zheng et al. (2022).

Sample MW19-79A that shows clear indication for right lateral deformation comes from the vicinity of the NW fault plane (Fig. 6e, f, g). Ages for the four fractions vary between 6.9 and 21.2 Ma, while proportion in $2M_1$ illite varies between 0 and 54.08 % (Table S2-3). York regression of the four ages with respect to the $2M_1$ percentage yield a 6.5 ± 0.7 Ma age at the lower (0%) intercept, and 34.8 ± 3.1 Ma at the upper (100%) intercept (Fig. 7).

MW19-79E sampled in the black gouge in vicinity of the SE fault plane yield ages between 9.6 and 60.2 Ma, while proportion in $2M_1$ illite varies between 5.64 and 51.5 % (Table. S2-3). Regression of the four ages yield 7.3 ± 2.8 Ma at the lower intercept, and 109.2 ± 12.4 Ma at the upper one (Fig. 7).

XRD analysis of both samples show that the only K-bearing minerals are illite (Table S2-1). Illites are strongly oriented by the right-lateral deformation (Fig. 6g, h). For both sample the apparent ages decrease linearly with the $2M_1$ illite (inherited) content, and the two lower intercepts are identical within error while the two upper intercept ages are clearly distinct. We interpret this as reflecting a single $1M_d$ (authigenic) growth event at 6.9 ± 2.9 Ma (upper Miocene) affecting two distinct host rocks that yield ages of 109.2 ± 12.4 Ma in the SE and 34.8 ± 3.1 Ma in the NW. The fault gouge results from brittle deformation of the host/parent rocks at temperature ≤ 200 °C, and crystallization of illite in fault gouge occurs between 110 °C and 180 °C (Duvall et al., 2011; Mottram et al., 2020). We thus interpret the $1M_d$ growth event as resulting from motion along the brittle WM fault, and the ages as yielding a minimum age for the onset of that fault. The fact that the ages record a common resetting age, but a distinct inherited component precludes temperature to have exceeded ~260°C after faulting (Hunziker et al., 1986).

4.2 White mica $^{40}Ar/^{39}Ar$ dating

$^{40}Ar/^{39}Ar$ is applicable to *in situ* dating of fabric-forming minerals, particularly white micas crystallized (or recrystallized) in schistose and mylonitic rocks (Di Vincenzo et al., 2016, Laurent et al., 2021). Combined with conventional step-heating, the technique can provide temporal constraints on deformation stages recorded by composite fabrics formed near the brittle-viscous transition at greenschist-grade conditions (Beaudoin et al., 2020). We present *in situ* laser and step heating $^{40}Ar/^{39}Ar$ dating of white mica for sample MW19-38A showing top to the SE deformation (Fig. 5c), and MW19-10B showing top to the NW deformation (Fig. 5f). Details on the technique are given in S3, structural information is reported in table 1.

Micaschist MW19-38A was collected in Paleozoic metamorphic rocks with S/C relationships indicating top to the SE (reverse) deformation ~200 m NW of the brittle WM fault (Fig. 4a). Ductile quartz, white mica and chlorite layers constitute the shear bands but feldspar porphyroclasts are brittlely deformed (Fig. 5c). This suggests deformation temperature < 450 °C (Sibson 1992), more probably close to 310-350°C (Stöckhert et al., 1999). Using Bourdelle and Cathelineau (2015) thermometer that is accurate for temperatures ≤350 °C, chlorite composition yield temperature estimates between 170 and ≥350 °C, with most data (46%) at ~ 350°C (Fig. S11; table S11-1).

Quantitative composition maps of the white mica (see S8 for the analytical procedure) shows two generations of white mica based on their celadonite (Xcel) content. One has Xcel < 0.2, while the other has higher Xcel up to 0.4 (Fig. 8a) (Fig. S4-1). In situ $^{40}Ar/^{39}Ar$ dating yield apparent ages between ~10 and 600 Ma with most ages ≤ 30 Ma (Figs. 8a, c, S4-1, S4-2; Table S4-1). White micas with low Xcel (Xcel < 0.2) have younger apparent ages (< 20 Ma) than the ones with higher Xcel (> 300 Ma). Among the youngest ages, forty-nine spots define an average of 15.4 ± 0.2 Ma (MSWD = 1.35) (Fig. 8c). The companion step heating runs yield relatively flat age spectra with ages between 10 and 23 Ma, with a large fraction of the ages consistent with the young in situ component at ~15 Ma (Fig. 8c, Table S5). Our interpretation is that the micas with Xcel > 0.3 are porphyroclasts inherited from an early event (≥ 600 Ma) while the younger age of the Xcel < 0.2 micas record a younger fluid-rock interaction event responsible for the growth of secondary white micas and chlorite between 250 and 350 °C during top to the east deformation. That temperature is lower than the closure temperature of white micas for the K/Ar system of 400-445 °C (Harrison et al., 2009) and recently revised theoretical and empirical estimates (Nteme et al., 2022, 2023) implying that the 15.4 ± 0.2 Ma (middle Miocene) age correspond to white mica crystallization, not cooling.

Micaschist MW19-10B from ~200 m SE of the brittle WM fault (Fig. 4a) shows top-to-NW right-lateral / normal shear planes underlined by recrystallized quartz and white mica (Fig. 5f). Chemical composition of the white mica shows moderate variation in Xcel content between 0.2 and 0.4 % (Fig. 8b; S6-1a). Chlorite compositions yield temperature estimates between 315 and ≥350 °C, with one outlier at 160 °C, and most data (37%) at ~350°C (Fig. S11; table S11-1). In that part of the Pengguan range RSCM data east of the WM fault suggest that temperature never exceeded 360 °C (Airaghi et al., 2018a). In situ $^{40}Ar/^{39}Ar$ dating yield apparent ages between 30 and 140 Ma (Fig. 8b, d, S6-1, Table S7). The step-heating spectrum displays a flat (concordant) segment at 28.0 ± 0.9 Ma in the early gas release (4% to 48% of the total ^{39}Ar), consistent with the youngest component of the in-situ data (Fig. 8d, Table S7). Step-ages then climb up to ~450 Ma, indicating an inherited high-temperature component. Our interpretation is that the top to the NW (normal / right lateral) ductile deformation occurred at 300-360 °C inducing feldspar deformation and chlorite and white mica (re)-crystallization at 28.0 ± 0.9 Ma (Middle Oligocene), while a previous metamorphic event occurred at ≥140 Ma. This deformation age is fully consistent within error with the $^{40}Ar/^{39}Ar$ step-heating age of 26.2 ± 1.0 Ma inferred to date normal deformation from white micas sampled less than 1 km away (Xue et al., 2021). The deformation temperature is below the 400-445 °C closure temperature of white micas for the K/Ar system, implying crystallization rather cooling age (see above).

5 Discussion

5.1 Timing of brittle and ductile deformation in the WM fault zone

Fault gouge K/Ar dating at site MW19-79 indicates that brittle faulting was ongoing along the WM fault at 6.9 ± 2.9 Ma (~7 Ma, upper Miocene). Such faulting is

dominantly right lateral with a slight reverse component (pitch between 10° and 40° S). Our $^{40}Ar/^{39}Ar$ data indicate that top to the east (reverse) deformation occurred in the Paleozoic schists at 15.4 ± 0.2 Ma (~15 Ma, middle Miocene), while top to the northwest (normal / right lateral) took place at the margin of the Pengguan complex at 28.0 ± 0.9 Ma (~28 Ma, Middle Oligocene).

The right-lateral fault kinematics with a slight reverse component are compatible with the ~25 km right-lateral offset of the river network (Fig. 3) and the higher altitude of the Xuelongbao complex with respect to the Pengguan (Fig. 1c).

The ductile top the east (reverse) shear along the WM fault zone is usually ascribed to the amphibolite-grade deformation that affected the whole Paleozoic metasediments north of the Pengguan range during the Upper Triassic and created the nappes in the external part of the Longmen Shan (Airaghi et al., 2018a; Xue et al., 2021). Our age of deformation at 15.4 ± 0.2 Ma points to a clearly much younger event (middle Miocene) of reverse shear restricted to the WM fault zone between the Xuelongbao and Pengguan ranges (see below).

The age of top to NW (normal) shear along the NW boundary of the Pengguan range was poorly constrained so far and some have proposed that it could correspond to a major detachment fault (Wang et al., 2014). Based on three white mica $^{40}Ar/^{39}Ar$ age spectra, Xue et al. (2021) proposed that deformation occurred episodically at 141–120 Ma, 81–47 Ma, and 27–25 Ma. These Cretaceous and Paleocene ages are deduced from complex age spectra possibly affected by mixed ages (partial resetting), in the same way as the older components seen in our data (cf. Section 4.2). In contrast, our *in situ* approach clearly resolves, and confirms, their Middle Oligocene age with a robust estimate at 28.0 ± 0.9 Ma. This Miocene age is further compatible with the exhumation histories of the Pengguan and Xuelongbao ranges (see below).

5.2 Differential uplift across the WM fault zone

Independent but complementary to direct dating of faults and mylonite, quantitative kinematics can be deduced from thermochronological modelling of cooling due to exhumation in the hanging (thrust) or footwall (normal fault) of fault systems.

During the lower Cretaceous, the Pengguan massif experienced a metamorphic event at conditions of 7 ± 1 kbar, 280 ± 30 °C (Airaghi et al., 2017). Low-temperature thermochronological data (ZHe, AFT, and AHe) staggered over more than 3000 m of differential height within the Pengguan range further constrain the range cooling history suggesting that slow, steady exhumation during early Cenozoic was followed by two pulses of rapid exhumation, one beginning 30–25 Myr ago and a second 10–15 Myr ago and still active today (Godard et al., 2009; Kirby et al., 2002; Wang et al., 2012) (Fig. 9). The temperature conditions estimated for sample MW19-10B at ~28 Ma appear to be ~100 °C higher than the cooling path of the Pengguan (Wang et al., 2012) (Fig. 9). This is probably because that path is inferred from samples located in the central and eastern Pengguan far away from the WM fault while MW19-10B is from the fault zone close to the Pengguan.

West of the WM fault, the Upper Triassic – Lower Jurassic metamorphism (11 ± 2 kbar and ~620 °C) (Dirks et al., 1994; Airaghi et al., 2018b; 2019; Xue et al., 2021)

was followed by ~2-4 km exhumation in the Early Cretaceous (~120-135 Ma) (Li et al., 2023) (Fig. 9). Cooling / exhumation resumed in the Cenozoic and Tian et al., (2013) interpreted faster Late Cenozoic exhumation rates deduced from ZHe ages in the Xuelongbao than in the Pengguan as due to out of sequence thrusting on the WMF. This was confirmed by Shen et al. (2019) who, using Pecube-based inverse modelling of ZFT, ZHe, and AHe data from two transect spanning ~3300 m in elevation in the Xuelongbao, infer an exhumation rate of 0.9 – 1.2 mm/yr from ~13 Ma to present. Inverse 1D modelling using the TQTec code of ZFT, AFT, and AHe data spanning nearly 3900 m of altitude, lead Furlong et al. (2021) to propose a more complex history with an earlier start of exhumation at ~27 Ma, a fast exhumation at 2 mm/yr between 17 - 15 Ma and a final stage at ~1 mm/yr since ~6 Ma (Fig. 9). The temperature conditions estimated for sample MW19-38A are compatible with that cooling history (Fig. 9).

Both the Xuelongbao and Pengguan massif appear to share a nearly identical onset of Cenozoic exhumation at ~30 Ma (Fig. 9), pointing to a major regional event. Exhumation of the Xuelongbao massif (~16 km) is however significantly greater than that of the Pengguan Massif (~10 km). Analysis of the differential exhumation between both massifs allows the timing and rate of vertical motion on the WM fault zone to be discussed. The differential vertical rates across the west dipping WM fault zone calculated from the more likely models of Wang et al. (2012) for Pengguan and Furlong et al. (2021) for Xuelongbao (Fig. 9) indicate four main kinematic stages (Fig. 10a). 1) A normal motion at the onset of global exhumation (~30 Ma) until ~25 Ma, with a vertical rate between 0.79 and 0.40 mm/yr (~3.2 km of relative subsidence of the Xuelongbao). 2) A reverse motion until ~15 Ma, with a maximum rate of 1.93 mm/yr (relative uplift of ~6.3 km). 3) Negligible vertical motion until ~6 Ma at ≤ 0.26 mm/yr. 4) Reverse motion since ~6 Ma at 0.72 mm/yr (relative uplift of ~4.2 km). The timing of these relative vertical motions is strikingly similar to the deformation style and absolute timing found in this study in at least three respects.

First, the age of brittle faulting at ~7 Ma closely matches the final exhumation starting at ~6 Ma. Since 6 Ma, the total exhumation of Xuelongbao would be of ~7 km, ~5 km greater than Pengguan (Furlong et al., 2021). Preservation of the 25 km right-lateral offset of the river network despite erosion suggests that it dates back to the onset of the last exhumation event in the hanging wall (i.e. ~6 Ma). This would correspond to a horizontal strike-slip rate of ~4.2 mm/yr. Brittle motion on WM fault is mostly strike-slip but involves a significant uplift of the NW compartment. The pitch angle of the slickensides measured in the field (~11° S, Fig. 6c) is consistent with the direction of motion calculated assuming a vertical rate of ~0.72 mm/yr, a horizontal rate of 4.2 mm/yr, and a fault dip angle of 65°-70° (~12° S). The thrusting component is responsible for the exhumation of the western compartment (hence the entrenchment of the river network) following a ~9 yr long period of negligible exhumation. The actual strike-slip motion may have started slightly before the exhumation became substantial, possibly explaining why the apparent horizontal geological offset is slightly larger than the morphological one (27 vs 25 km) (Figs. 3b, S1-1b).

Second, the Miocene phase of reverse faulting starting at ~25 Ma peaked at 1.93 mm/yr around 16.6-14.8 Ma, coinciding with the 15.4 ± 0.19 Ma age of reverse

motion recorded by our sample MW19-38A. Top to the east thrusting thus lasted until the middle Miocene (25-15 Ma) along the ductile WM fault zone to produce ~6.3 km more exhumation in Xuelongbao than in Pengguan. Given the average dip of the motion on the shear planes (45°, Fig. 4c), this corresponds to a shortening of ~6.3 km in the E-W direction.

Third, normal motion on the WM fault zone from ~30 Ma until ~25 Ma at a vertical rate of 0.79 – 0.4 mm/yr., is coeval with deformation ages of 28 ± 0.9 Ma (sample MW19-10B, this study) and 26.2 ± 1.0 Ma (sample CX2, Xue et al., 2021) associated with ductile normal/ right lateral deformation. Given the lineation attitude (Fig. 4d), the ~3.2 km of subsidence corresponds to ~2.7 km of stretching in the N350° direction (~50° dip). Such normal / right lateral motion on the WM fault zone resulted from differential motion with respect to Pengguan while both massifs were rising, most probably above a sole thrust corresponding to the Yingxiu-Beichuan and Wenchuan-Maoxian faults.

5.3 Cenozoic faulting and building of Longmen Shan

The kinematic history of the WM fault zone discussed above shed new light on the Longmen Shan tectonics during the Cenozoic and the accompanying deformation / uplift mechanisms.

The onset of exhumation of central Longmen Shan in the Oligocene (~30 Ma) is interpreted as due to thrusting on a sole thrust dipping to the NW, presumably the Yingxiu-Beichuan fault (Hubbard and Shaw, 2009; Wang et al., 2012; Shen et al., 2019). A similar timing of exhumation is reported at other locations along the eastern Tibetan margin (Cao et al., 2019, Zhu et al., submitted). This led Zhu et al. (submitted) to propose that a ~500 km long thrust fault, the Yulong-Muli-Jinpingshan-Longmenshan (YMJL) bounded eastern Tibet before being offset by the Xianshuihe strike-slip fault. Normal motion with a large right-lateral component occurred along the WM fault zone at that time. As we show, this was linked to differential uplift, whose effective cause needs to be elucidated yet. What is clear however, is that since the onset of Cenozoic building of the Tibetan plateau, the WM fault never experienced pure normal motion, and no normal motion at all since the Oligocene.

The total Cenozoic exhumation of the Xuelongbao is ~16 km (Furlong et al., 2021). Significant top to the east thrusting occurred during the middle Miocene (27-15 Ma) along the ductile WM fault zone inducing ~13 km of exhumation (Furlong et al., 2021) in the internal part of the Longmen Shan. At that time, exhumation (and thus probably thrusting above the sole thrust) was slower in the externally located Pengguan massif. This implies out-of-sequence thrusting with respect to the previous activation of the sole thrust in the Oligocene. Thrusting on the frontal Guanxian-Anxian and Yingxiu-Beichuan is still active as shown by the Wenchuan earthquake (Fig. 1b) implying that the main locus of thrusting has migrated back to the frontal part. This implies a more complex organization of thrusting on the eastern Tibet margin than a classical external propagation model would suggest, as already proposed for the Yalong margin further south (Pitard et al., 2021; Zhu et al., submitted). This kind of thrusting pattern could be linked to the steepness of faults

such as the WM fault zone, and possibly also to a significant strike-slip component of motion. The steepness of the thrust could also explain the absence of significant flexural basin.

The recent kinematics of the WM fault are characterized by right-lateral shear with a reverse component. Such motion is consistent with the 2008 Mw7.9 Wenchuan main shock focal mechanism (USGS) which has been documented on a NE-SW striking NW dipping fault, and Yingxiu-Beichuan surface ruptures (Fu et al., 2011) (Fig. 1b). This indicates that present-day kinematics of these major faults in Longmen Shan are comparable to those having prevailed during the upper Miocene. However, the absence of surface break along the WM fault during the Wenchuan mega-earthquake suggests that it could be now inactive with right-lateral motion being transferred on the parallel and more external Yingxiu-Beichuan fault.

5.4 Cenozoic building of the Tibetan eastern margin: channel flow or crustal stacking?

Lateral extrusion of partially molten crustal material outward from below Tibet has been widely proposed to explain the steep boundaries of the Tibetan plateau. (e.g., Clark and Royden, 2000; Beaumont et al., 2001; Clark et al., 2005b; Cook and Royden, 2008; Adams and Hodges, 2022). In the Longmen Shan, the Pengguan metamorphic complex is composed of NeoProterozoic granites without any trace of Cenozoic melting. Crustal extrusion would result from growth of the deep crust in a weak layer pushing the Pengguan range and inducing thrusting along the Yingxiu-Beichuan fault and normal faulting along the WM fault (Fig. 2b) (e.g., Royden et al., 1997; Clark et al., 2005a; Burchfiel et al., 2008, Royden et al., 2008). However, we clearly document that the WM fault has not been normal since the Oligocene implying that extrusion at the front of a crustal channel flow did not occur in the Longmen Shan in the Cenozoic.

According to the rheology of the lower crust, numerical models of crustal channel flow do not necessarily imply extrusion of the crust at the surface but can result in tunnelling or formation of domes or nappes at depth (Beaumont et al., 2006; Jamieson et al., 2013). Some have proposed that the Longmen Shan thrust wedge would be pushed from bellow by a lower channel flow originated from below Tibet (Fig. 2c) (Zhang, 2013). Such hypothesis is difficult to test from geological observations at the surface. Zones of high electrical conductivity (Bai et al., 2010) and low shear wave speed (Li et al., 2009; Yao et al., 2008) in east Tibet appear to support Channel flow. Seismic tomography confirms that the Longmen Shan is an important boundary between the thick Songpan block with its LVZ's and the thinner and more rigid Sichuan crust (e.g., Li et al., 2009; Robert et al., 2010; Liu et al., 2014). However, other geophysical experiments revealed that the LVZ are not as continuous as previously envisaged and that present-day widespread channel flow appears dubious (e.g., Hetényi et al., 2011; Yao et al., 2010; Zhao et al., 2012; Li et al., 2014). Further analysis of geophysical images shows that the LVZs are within the Songpan Block and stop ~25 km west of the Longmen Shan (e.g., Zhao et al., 2012). Dragging of the upper crust should thus not occur below the Longmen Shan as inferred by Zhang (2013) model (Fig. 2c) but west of the WM fault where there is no reverse fault nor significant relief.

We conclude that crustal channel flow is not, and has not been at least since the Oligocene, the active mechanism that would have produced and maintained the steep LMS topography. The LMS rather results from crustal stacking in an accretionary

prism, with a large strike-slip component and out of sequence thrusting on steep thrusts.

6 Conclusions

Combining field analysis with direct deformation dating (K-Ar on fault gouge and $^{40}Ar/^{39}Ar$ on white micas) and thermochronology, we constrain the kinematics and exhumation history of the Wenchuan-Maowen (WM) fault zone that is key to decipher between the various models proposed for Cenozoic building of the eastern Tibetan plateau margin (Longmen Shan). The WM fault zone records onset of exhumation of the Longmen Shan in the Cenozoic with various steps across the viscous/brittle regime during progressive exhumation. Coupled structural analysis and in situ dating shows that, at the onset of exhumation in the Middle Oligocene (~30 - 25 Ma), the fault was right-lateral /normal while thrusting was taking place on a deeper, more external part of the Yulong-Muli-Jinpingshan-Longmenshan thrust belt. In the middle Miocene (25-15 Ma), out-of-sequence thrusting along the WM fault zone was active while thrusting on the basal thrust was decelerating, inducing ~6 km of differential exhumation between the Xuelongbao and Pengguan ranges. After a ~9 Myr pause, exhumation of the Xuelongbao resumed during the upper Miocene (~6 Ma) with the activation of the brittle right lateral / reverse WM fault that accrued ~25 km of right lateral offset, now visible in the river network. Such deformation is still active in the Longmen Shan but it is unclear whether this is so across the WM fault today. The MW fault zone never showed pure normal motion, dismissing a lower crustal channel flow extrusion model for building what has often been considered as one archetype example of such mechanism: the east Tibet topographic step. This topography rather results from crustal shortening, including activation of steep out of sequence reverse faults with significant right-lateral component.

Acknowledgements

This work was supported by the National Science Foundation of China (41830217, 42072240, 41972229) and the China Geological Survey (DD20221630). The Ar/Ar lab at ISTO is supported by LABEX grant VOLTAIRE (ANR-10-LABX-100-01), the Région Centre grant ARGON, and the EQUIPEX grant PLANEX (ANR-11-EQPX-0036). We thank Lei Zhang, Thomas Courrier and Xiaozhou Ye for field assistance; and Marie-Luce Chevalier for discussion of fault horizontal offset. Two anonymous reviewers and the editor helped to clarify the manuscript.

Table 1
Samples location, structural information, Temperature estimates and dating results.

Site	Latitude	Longitude	Structure	Measurement	Sample	$^{40}Ar/^{39}Ar$ Age	K-Ar lower intercept Age	T estimate
MW19-10	31.075	103.315	Top-to-NW normal	Foliation N5, 72W Lineation Pitch: 37 N	MW19-10B	28.0 ± 0.9 Ma		300 - 350 °C
MW19-38	31.084	103.312	Top-to-E reverse	S foliation N23, 87W Lineation Pitch: 72N	MW19-38A	15.4 ± 0.2 Ma		250 - 350°C
				C foliation N24, 36W				
MW19-79	31.494	103.623	Dextral with reverse	Fault plane N58, 67W Slickenside Pitch: 10S	MW19-79A		6.5 ± 0.7 Ma	
				Fault plane N57, 65W Slickenside Pitch: 4[illegible]S	MW19-79E		7.3 ± 2.8 Ma	
MW19-11	31.078	103.312		Fault plane N[illegible]1, 68W				
MW19-81	31.574	103.722		Fault plane N25, 61W Slickenside Pitch: 64S				

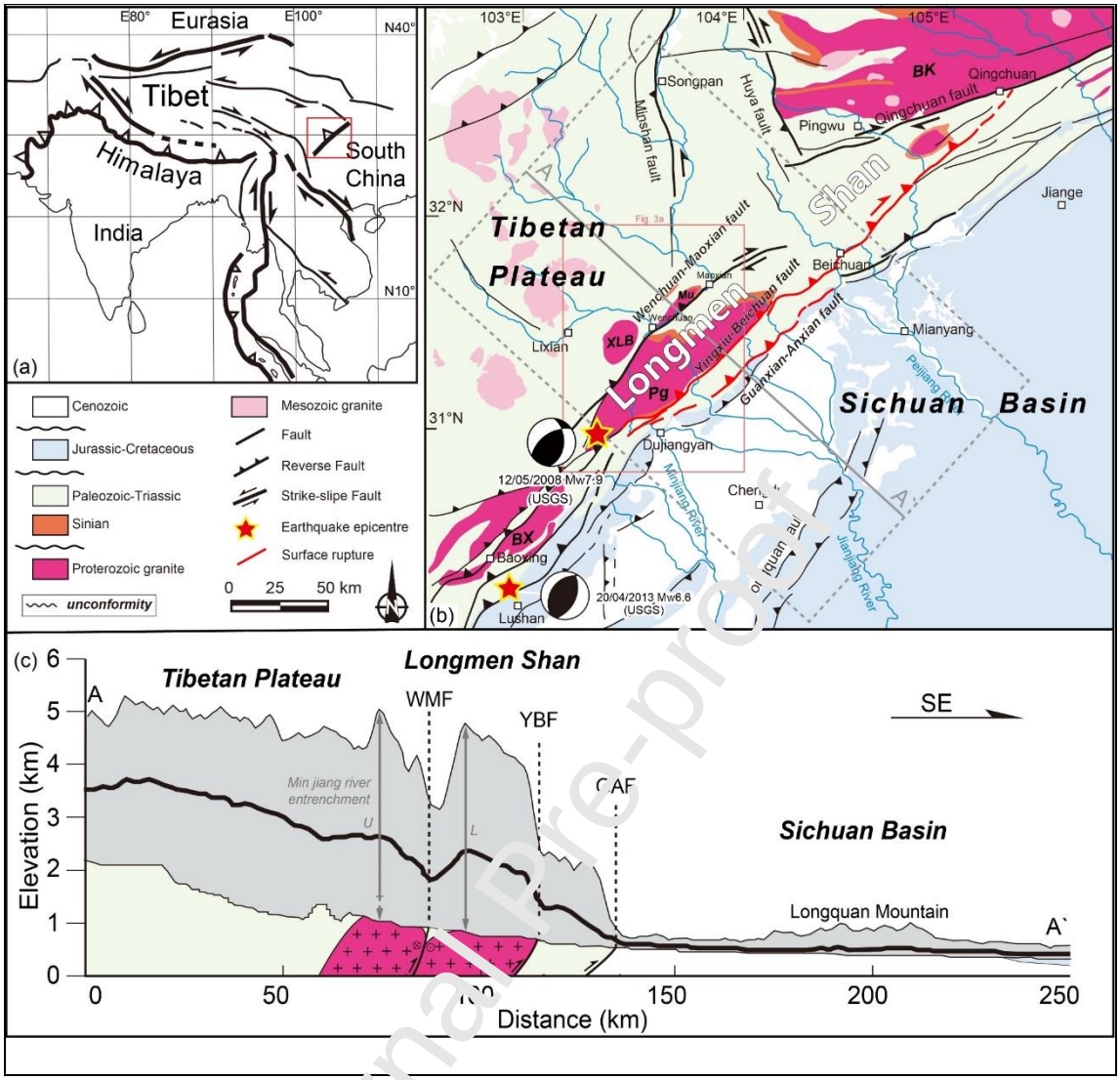

Fig. 1 The Longmen Shan belt (a) Location of the Longmen Shan in the frame of the India-Asia collision. (b) Geological map of Longmen Shan and adjacent area (modified from Li et al., 2014), with three major faults: Wenchuan-Maoxian (WMF), Yingxiu-Beichuan (YBF), and Guanxian-Anxian (GAF). Focal mechanisms of Wenchuan and Lushan Earthquakes are shown. Basement ranges: MT, Mutuo; XLB, Xuelongbao; PG, Pengguan; BX, Baoxing; BK, Bikou. (c) A-A' cross section. Grey frame is the topography (swath profile) with average (bold), upper and lower values. Simplified geological cross section at the bottom. Double arrows indicate the minimum entrenchment of the Min Jiang river: U, upper reach, L, Lower Reach.

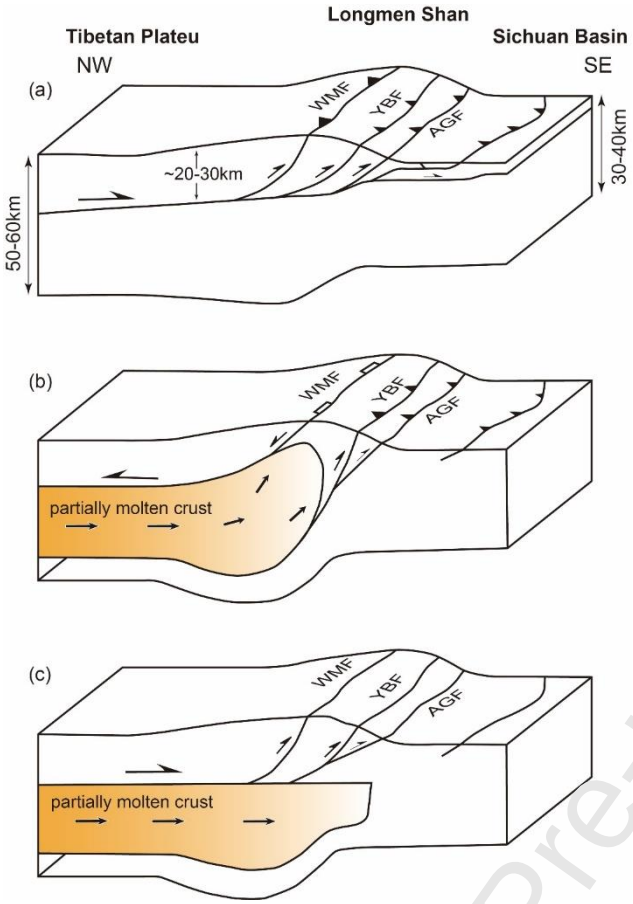

Fig.2 Conceptual models for the Cenozoic Longmen Shan evolution. Adapted from Tian et al., (2013).

a) Crustal thickening through reverse faulting (e.g., Hubbard and Shaw 2009)

b) Exhumation in front of a buoyant lower crust expelled from below the Tibetan plateau (channel flow extrusion) requiring a normal fault along the Wenchuan – Maoxian fault at the backside of the channel (e.g., Royden et al., 2008; Burchfiel et al., 2008).

c) A modified channel flow model. Flow of ductile lower crust drags the upper crust eastward to thicken the crust in the LMS through high-angle listric reverse faulting (e.g., Zhang, 2013).

WMF: Wenchuan – Maoxian fault, YBF: Yingxiu-Beichuan fault, GAF: Guanxian-Anxian fault. Note that surface topography is exaggerated.

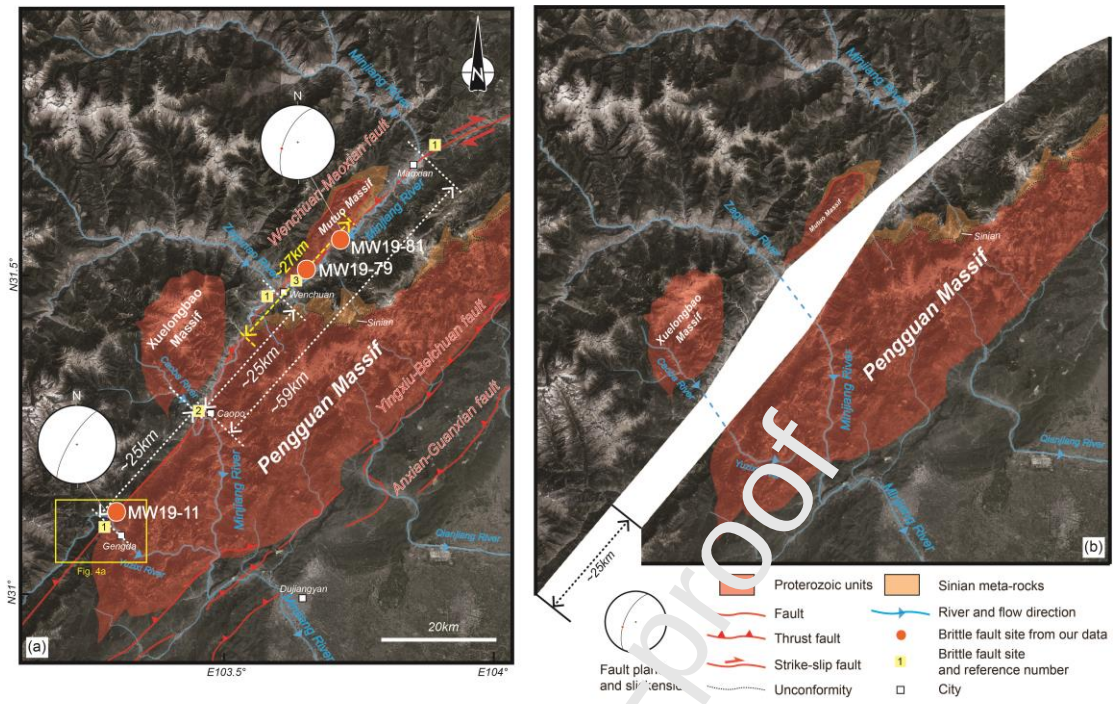

Fig. 3 The Wenchuan – Maoxian (WM) fault, geological offset and river network evolution. (a) Google earth image with major river channels, brittle faults and metamorphic complexes. River data are referenced and modified from GloRic dataset (Dallaire et al., 2019). Faults from Li et al. (2014) and personal mapping. Orange circles indicate brittle fault sites, stereplots show brittle fault attitude. Yellow squares and numbers indicate published brittle fault sites, 1: Dirks et al., 1994; 2: Airaghi, 2017; 3: Wang et al., 2014. (b) Reconstitution prior to right-lateral faulting assuming ~25 km right-lateral offset along the WM fault.

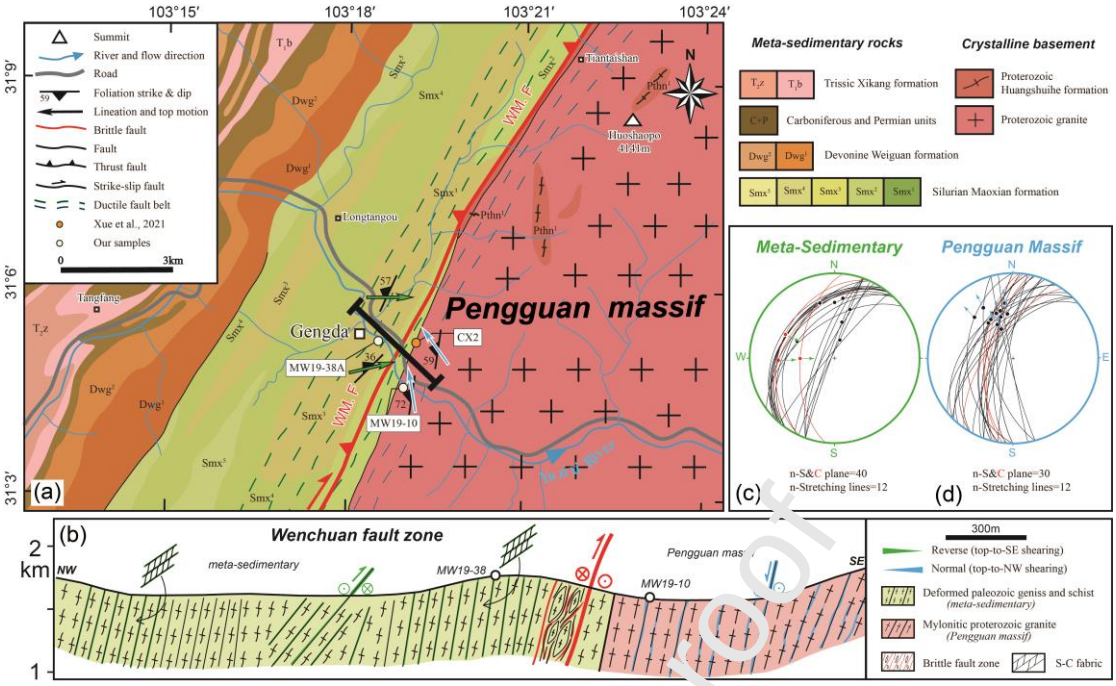

Fig. 4 Ductile deformation in the WM fault zone. a) Geological map of the Gengda area of the WM fault zone. See location on fig. 1b. b) Geological cross section through the WM fault and shear zones. c, d) Stereonet diagram of foliations and shear planes on the western side of the fault (c) and on the eastern side (d).

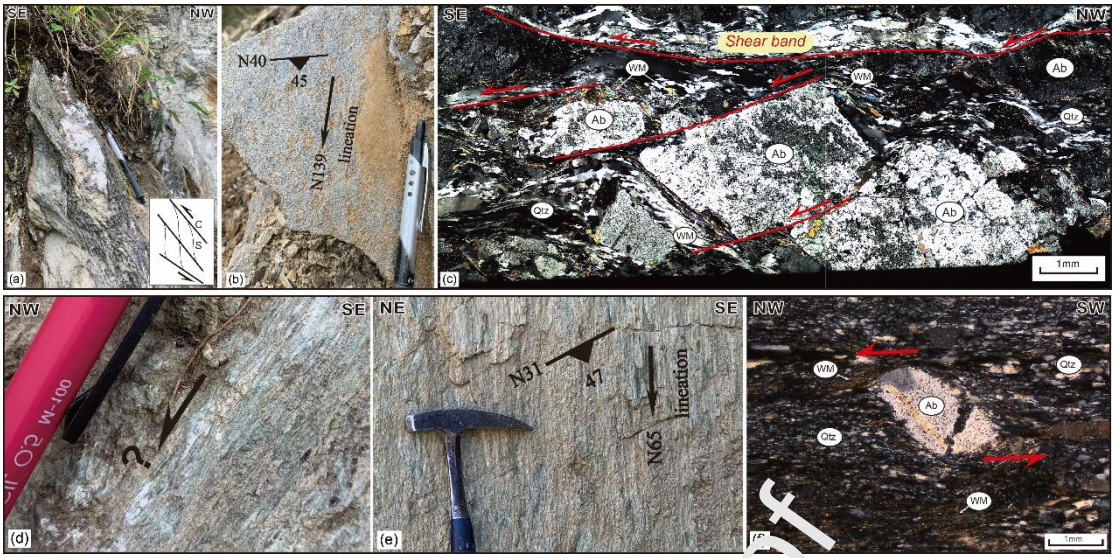

Fig. 5 Ductile deformed rocks of the WM shear zone. a - c) Top to the SE (reverse) deformation (site MW19-38A). a) S/C structure. b) Foliation and stretching lineation. c) Shear criteria in an oriented thin section of sample MW19-38A. d - f) Top to the NW (normal) deformation (site MW19-10B). d) Mylonitic foliation dipping to the NW. e) Stretching lineation view from above. f) Shear criteria in an oriented thin section of sample MW19-10B.

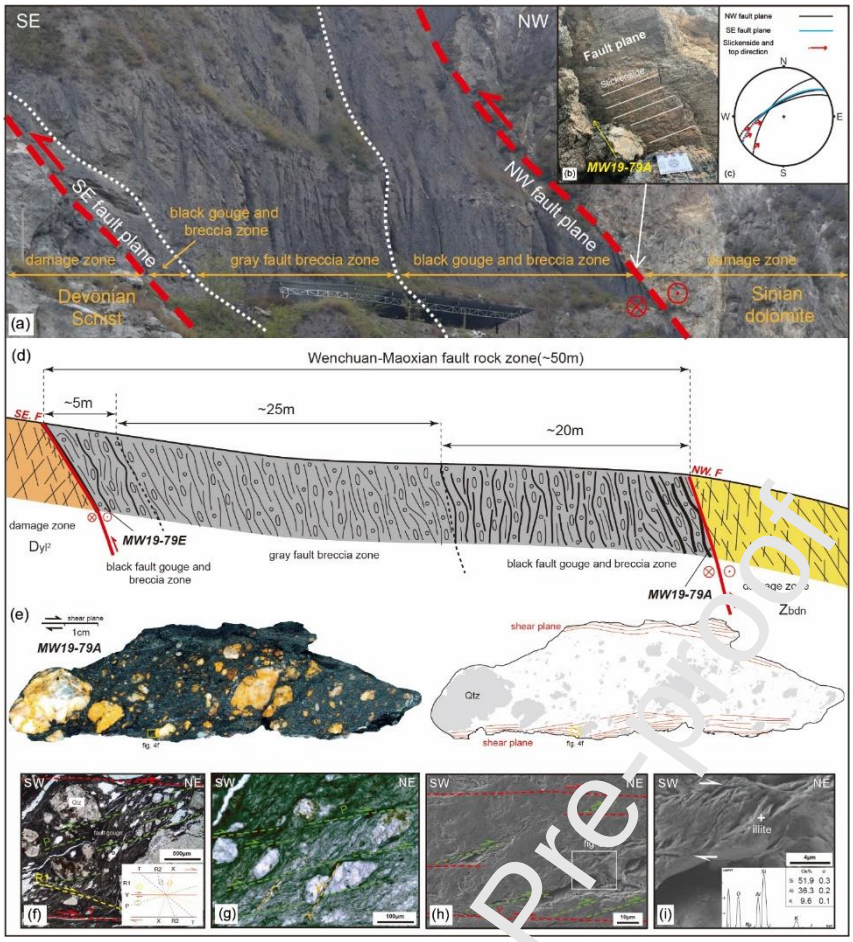

Fig. 6 Fault gouge of the Wenchuan-Maoxian fault at site MW19-79; (a) Picture of the fault zone outcrop (b) detail of the NW fault plane with sub-horizontal slickenside; (c) stereonet plot of fault planes and slickensides; (d) Fault zone cross-section showing samples location; (e, f, g, h, i) views of sample MW19-79A in the XZ plane showing "S/C" microstructures and Riedel shear elements at various scales implying right-lateral shear, red lines represent shear planes; (e, f, g) polished slab (h, i) SEM images. e) right is a line drawing of the picture on the left, with clasts in grey and shear planes in red; i) also shows the illite EDS spectrum.

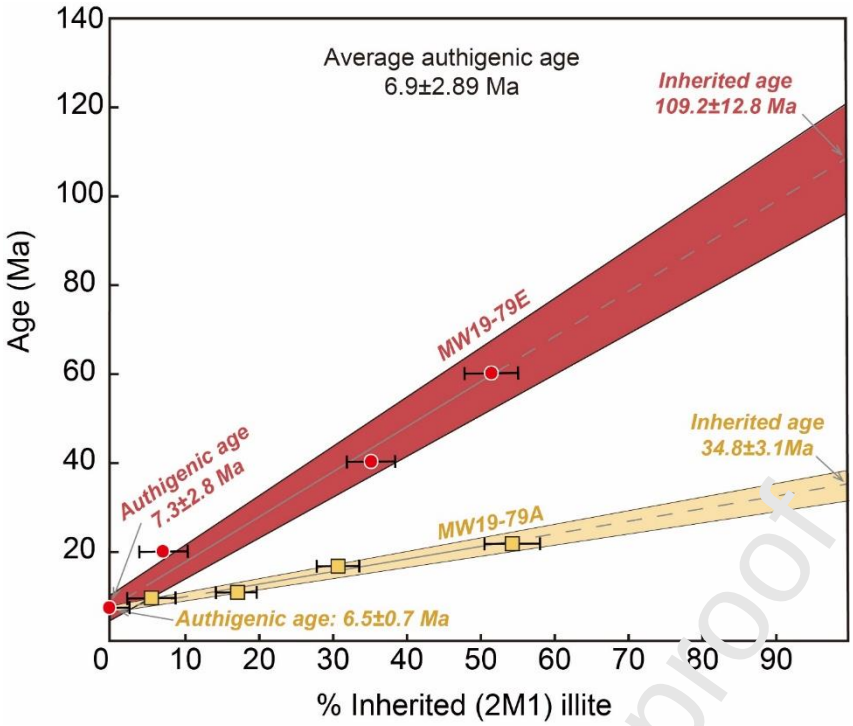

Fig. 7 Illite age plot of samples MW19-79A and MW19-79E.

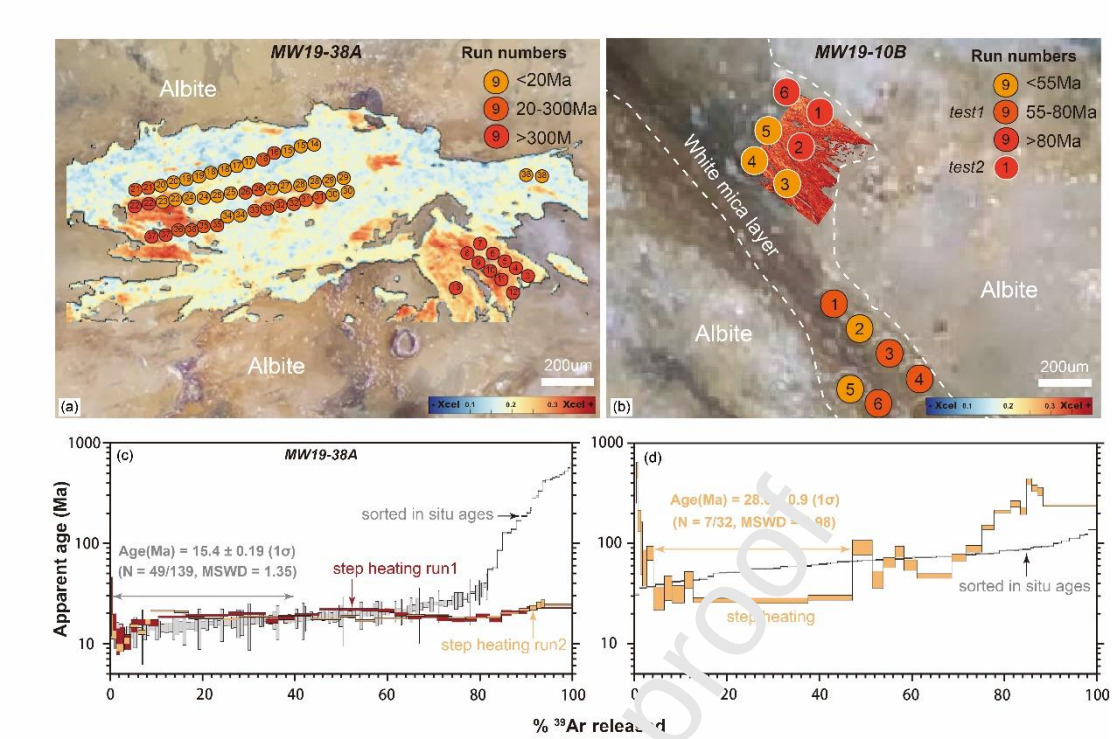

Fig. 8 $^{40}Ar/^{39}Ar$ dating results of ductile deformation of samples MW19-38A (a and c), and MW19-10B (b and d). (a) and (b) in situ laser ablation map with spot numbers. Spot colours refer to apparent ages. The background is thin section (reflective light) or chemical composition (X Celadonite) when available. c) age spectra (two runs) and sorted in situ ages of sample MW-38A. d) age spectra and sorted in situ ages of sample MW-10B.

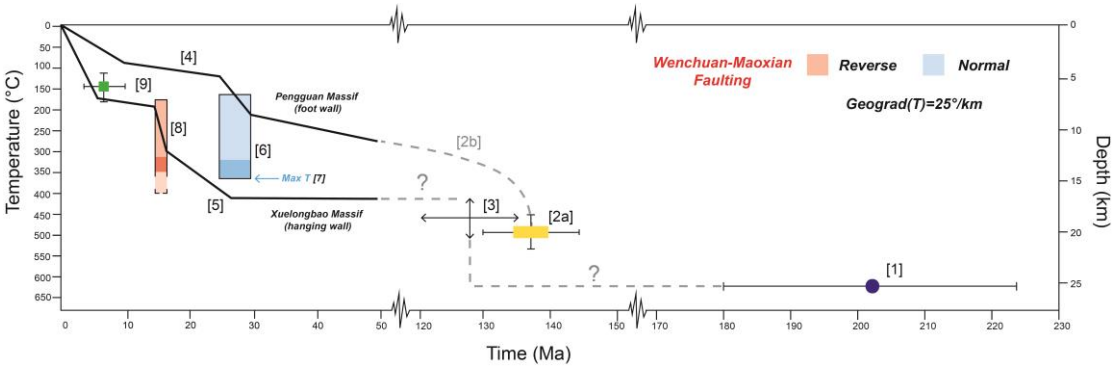

Fig. 9 Exhumation – cooling history of the Pengguan and Xuelongbao massifs. [1] P-T estimate of Lower Jurassic metamorphism in Xuelongbao (Airaghi et al., 2018b). [2a] Lower Cretaceous P-T estimate (Airaghi et al., 2017), and [2b] Lower Cretaceous cooling path (Airaghi et al., 2017) of Pengguan. [3] Amount of Early Cretaceous exhumation of Xuelongbao (Li et al., 2023). [4] Exhumation history of the Pengguan range (Wang et al., 2012). [5] Exhumation history of the Xuelongbao range (Tian et al., 2013; Furlong et al., 2021). [6]. Temperature estimate of the top to the northwest (right-lateral / normal) deformation (MW19-10B) (this study), with [7] maximum estimate from RSCM (Airaghi et al., 2018a). [8] Temperature estimate of top to the SE (reverse) deformation (MW19-38A) (This study). [9] Gouge formation at site MW19-79 (this study). Correspondence between depth and temperature assuming a geothermal gradient of 25°C/km.

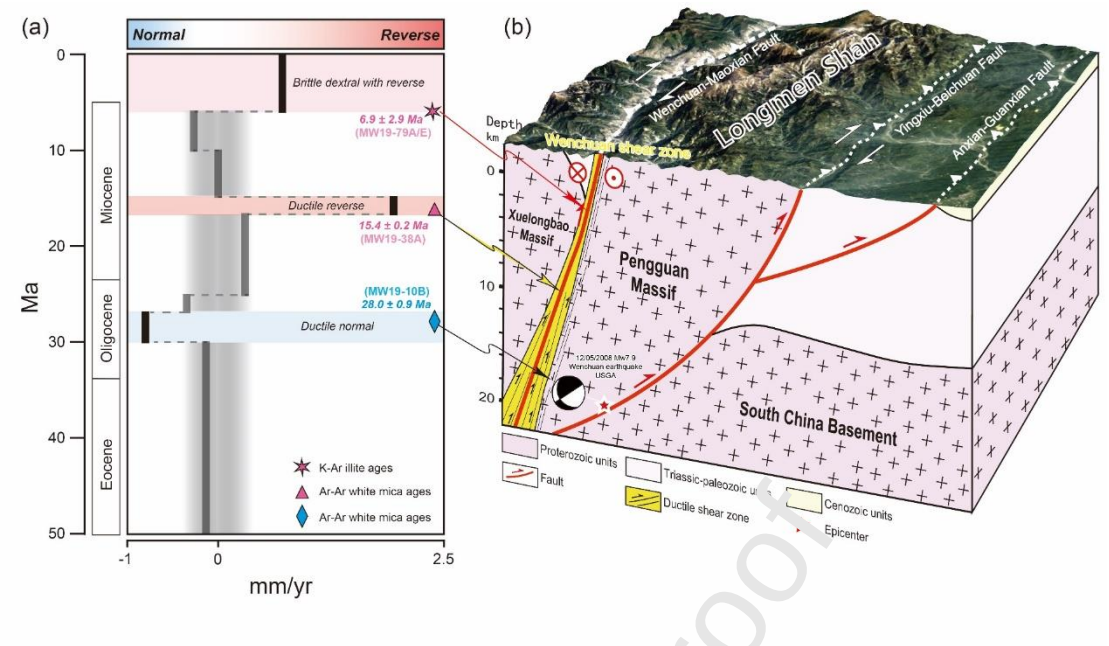

Fig. 10 Kinematics of the Wenchuan-Maowen fault. (a) vertical differential exhumation across the fault according to thermochronological data of the Pengguan and Xuelongbao ranges (Furlong et al., 2021; Wang et al., 2012). Negative values correspond to normal motion on the NW dipping fault, and positive to reverse motion. (b) structural bloc diagram of Longmen Shan in shallow crust.

Reference list

Adams, B. A.and K. V. Hodges. 2022. Potential Influences of Middle and Lower Crustal Flow on Landscape Evolution: Insights From the Himalayan-Tibetan Orogen. *Treatise on Geomorphology*. pp. 729-748. Academic Press.

Airaghi, Laura. 2017. Petro-chronological study of the Longmen Shan thrust belt (eastern Tibet) : geological inheritance and implication for the present geodynamics. Ph. D. Thesis, France

Airaghi, Laura, Julia de Sigoyer, Pierre Lanari, Stéphane Guillot, Olivier Vidal, Patrick Monié, Benjamin Sautter, and Xibin Tan. 2017. Total exhumation across the Beichuan fault in the Longmen Shan (eastern Tibetan plateau, China): Constraints from petrology and thermobarometry. Journal of Asian Earth Sciences. 140, 108-21.

Airaghi, L., De Sigoyer, J., Guillot, S., Robert, A., Warren, C. J., and Deldicque, D. 2018a. The Mesozoic along-strike Tectonometamorphic segmentation of Longmen Shan (eastern Tibetan plateau). *Tectonics*, *37* (12), 4655-4678.

Airaghi, Laura, Clare J. Warren, Julia de Sigoyer, Pierre Lanari, and Valérie Magnin. 2018b. Influence of dissolution/reprecipitation reactions on metamorphic greenschist to amphibolite facies mica40Ar/39Ar ages in the Longmen Shan (eastern Tibet). Journal of Metamorphic Geology. 36, 933-58.

Airaghi, Laura, Emilie Janots, Pierre Lanari, Julia de Sigoyer, and Valérie Magnin. 2019. Allanite Petrochronology in Fresh and Retrogressed Garnet–Biotite Metapelites from the Longmen Shan (Eastern Tibet). Journal of Petrology. 60, 151-76.

Arne, Dennis, Brenton Worley, Christopher Wilson, She Fa Chen, David Foster, Zhi Li Luo, Shu Gen Liu, and Paul Dirks. 1997. Differential exhumation in response to episodic thrusting along the eastern margin of the Tibetan Plateau. Tectonophysics. 280, 239-56.

Bai, D., Unsworth, M. J., Meju, M. A., Ma, X., Teng, J., Kong, X., and Liu, M. 2010. Crustal deformation of the eastern Tibetan plateau revealed by magnetotelluric imaging. *Nature geoscience*, *3*(5), 358-362.

Beaudoin, A., S. Scaillet, N. Mora, L. Jolivet, and R. Augier. 2020. In Situ and Step-Heating (40)Ar/(39)Ar Dating of White Mica in Low-Temperature Shear Zones (Tenda Massif, Alpine Corsica, France). Tectonics. 39.

Beaumont, C, Rebecca Anne Jamieson, MH Nguyen, and B Lee. 2001. Himalayan tectonics explained by extrusion of a low-viscosity crustal channel coupled to focused surface denudation. Nature. 414, 738-42.

Beaumont, C., Nguyen, M. H., Jamieson, R. A., & Ellis, S. 2006. Crustal flow modes in large hot orogens. *Special Publication-Geological Society Of London*, *268*, 91.

Bergmann, J., P. P. Friedel, and R. Kleeberg. 1998. BGMN - A new fundamental parameters based Rietveld program for laboratory X-ray sources, it's use in quantitative analysis and structure investigations.

Bollinger, L., Henry, P., and Avouac, J. P. .2006. Mountain building in the Nepal Himalaya: Thermal and kinematic model. Earth and Planetary Science Letters, 244(1-2), 58-71.

Bourdelle, Franck, and Michel Cathelineau. 2015. Low-temperature chlorite geothermometry: a graphical representation based on a T–R2+ –Si diagram. European Journal of Mineralogy. 27, 617-26.

Burchfiel, B. C., Chen Zhiliang, Liu Yupinc, and L. H. Royden. 1995. Tectonics of the Longmen Shan and Adjacent Regions, Central China. International Geology Review. 37, 661-735.

Burchfiel, B. C., L. H. Royden, R. D. van der Hilst, B. H. Hager, Z. Chen, R. W. King, C. Li, J. Lü, H. Yao, and E. Kirby. 2008. A geological and geophysical context for the Wenchuan earthquake of 12 May 2008, Sichuan, People's Republic of China. GSA Today. 18.

Cao, Kai, Guocan Wang, Philippe Hervé Leloup, Gweltaz Mahéo, Yadong Xu, Pieter A. van der Beek, Anne Replumaz, and Kexin Zhang. 2019. Oligocene-Early Miocene Topographic Relief Generation of Southeastern Tibet Triggered by Thrusting. Tectonics. 38, 374-91.

Clark, M.K., L.H Royden. 2000. Topographic ooze: Building the eastern margin of Tibet by lower crustal flow. Geology 28, 703–706.

Clark, Marin. K., House, M. A., Royden, L. H., Whipple, K. X., Burchfiel, B. C., Zhang, X., and Tang, W. 2005a. Late Cenozoic uplift of southeastern Tibet. Geology. 33(6), 525-528.

Clark, Marin K., John W. M. Bush, and Leigh H. Royden. 2005b. Dynamic topography produced by lower crustal flow against rheological strength heterogeneities bordering the Tibetan Plateau. Geophysical Journal International. 162, 575-590.

Clauer, Norbert. 2013. The K-Ar and $^{40}Ar/^{39}Ar$ methods revisited for dating fine-grained K-bearing clay minerals. Chemical Geology. 354, 163-85.

Cook, K.L., and L.H.,Royden. 2008. The role of crustal strength variations in shaping orogenic plateaus, with application to Tibet. Journal of Geophysical Research –Solid Earth 113. http://dx.doi.org/10.1029/2007JB005457.

Dallaire, Camille Ouellet, Bernhard Lehner, Roger Sayre, and Michele Thieme. 2019. A multidisciplinary framework to derive global river reach classifications at high spatial resolution. Environmental Research Letters. 14, 024003.

Densmore, Alexander L, Yong Li, Michael A Ellis, and Rongjun Zhou. 2005. Active tectonics and erosional unloading at the eastern margin of the Tibetan Plateau. Journal of Mountain Science. 2, 146-54.

Di Vincenzo, Gianfranco, Antonietta Grande, Giacomo Prosser, William Cavazza, and Peter G. DeCelles. 2016. $^{40}Ar-^{39}Ar$ laser dating of ductile shear zones from central Corsica (France): Evidence of Alpine (middle to late Eocene) syn-burial shearing in Variscan granitoids. Lithos. 262, 369-83.

Dirks, P.H.G.M., CJL Wilson, Shefa Chen, ZL Luo, and Shugen Liu. 1994. Tectonic evolution of the NE margin of the Tibetan Plateau; evidence from the central Longmen Mountains, Sichuan Province, China. Journal of Southeast Asian Earth Sciences. 9, 181-92.

Duvall, Alison R., Marin K. Clark, Ben A. van der Pluijm, and Chuanyou Li. 2011. Direct dating of Eocene reverse faulting in northeastern Tibet using Ar-dating of fault clays and low-temperature thermochronometry. Earth and Planetary Science Letters. 304, 520-26.

Feng, Shaoying, Peizhen Zhang, Baojin Liu, Ming Wang, Shoubiao Zhu, Yongkan Ran, Weitao Wang, Zhuqi Zhang, Wenjun Zheng, Dewen Zheng, Huiping Zhang, and Xiao-feng Tian. 2016. Deep crustal deformation of the Longmen Shan, eastern margin of the Tibetan Plateau, from seismic reflection and Finite Element modeling. Journal of Geophysical Research: Solid Earth. 121, 767-87.

Furlong, Kevin P., Eric Kirby, C. Gabriel Creason, Peter J. J. Kamp, Ganqing Xu, Martin Danišík, Xuhua Shi, and Kip V. Hodges. 2021. Exploiting Thermochronology to Quantify Exhumation Histories and Patterns of Uplift Along the Margins of Tibet. Frontiers in Earth Science. 9.

Gaudemer, Y, P Tapponnier, and DL Turcotte. 1989. River offsets across active strike-slip faults. Ann. tecton. 3, 55-76.

Godard, V., J. Lavé, J. Carcaillet, R. Cattin, D. Bourlès, and J. Zhu. 2010. Spatial distribution of denudation in Eastern Tibet and regressive erosion of plateau margins. Tectonophysics. 491, 253-74.

Godard, V., R. Pik, J. Lavé, R. Cattin, B. Tibari, J. de Sigoyer, M. Pubellier, and J. Zhu. 2009. Late Cenozoic evolution of the central Longmen Shan, eastern Tibet: Insight from (U-Th)/He thermochronometry. Tectonics. 28.

Harrison, M.T., Célérier, J., Aikman, A.B., Hermann, J., Heizler, M.T., 2009. Diffusion of 40Ar in muscovite. Geochim. Cosmochim. Acta 73, 1039–1051.

Haines, Samuel H., and Ben A. van der Pluijm. 2008. Clay quantification and Ar–Ar dating of synthetic and natural gouge: Application to the Miocene Sierra Mazatán detachment fault, Sonora, Mexico. Journal of Structural Geology. 30, 525-38.

Hetényi, G., Vergne, J., Bollinger, L., and Cattin, R., 2011. Discontinuous low-velocity zones in southern Tibet question the viability of the channel flow model. Geological Society, London, Special Publications. 353(1), 99-108.

Hubbard, J., and J. H. Shaw. 2009. Uplift of the Longmen Shan and Tibetan plateau, and the 2008 Wenchuan (Mw = 7.9) earthquake. Nature. 458, 194-7.

Hubbard, J., J. H. Shaw, and Y. Klinger. 2010. Structural Setting of the 2008 Mw 7.9 Wenchuan, China, Earthquake. Bulletin of the Seismological Society of America. 100, 2713-35.

Hunziker, JC, Martin Frey, Norbert Clauer, RD Dallmeyer, H Friedrichsen, W Flehmig, K Hochstrasser, P Roggwiler, and H Schwander. 1986. The evolution of illite to muscovite: mineralogical and isotopic data from the Glarus Alps, Switzerland. Contributions to Mineralogy Petrology. 92, 157-80.

Jamieson, R. A., Beaumont, C., Medvedev, S., & Nguyen, M. H. 2004. Crustal channel flows: 2. Numerical models with implications for metamorphism in the Himalayan-Tibetan orogen. *Journal of Geophysical Research: Solid Earth*, *109*(B6).

Jamieson, R. A., and Beaumont, C. 2013. On the origin of orogens. *Geological Society of America Bulletin*, *125*(11-12), 1671-1702.

Klemperer, S. L. 2006. Crustal flow in Tibet: geophysical evidence for the physical state of Tibetan lithosphere, and inferred patterns of active flow. Geological Society, London, Special Publications. 268(1), 39-70

Kirby, Eric, Peter W. Reiners, Michael A. Krol, Kelin X. Whipple, Kip V. Hodges, Kenneth A. Farley, Wenqing Tang, and Zhiliang Chen. 2002. Late Cenozoic evolution of the eastern margin of the Tibetan Plateau: Inferences from 40Ar/39Ar and (U-Th)/He thermochronology. Tectonics. 21, 1-20.

Kirby, E.and W. Ouimet, 2011. Tectonic geomorphology along the eastern margin of Tibet: Insights into the pattern and processes of active deformation adjacent to the Sichuan Basin. *Geological Society, London, Special Publications*, *353*(1), 165-188.

Kohn, M. J. 2008. PTt data from central Nepal support critical taper and repudiate large-scale channel flow of the Greater Himalayan Sequence. Geological Society of America Bulletin, 120(3-4), 259-273.

Laurent, Valentin, Stéphane Scaillet, Laurent Jolivet, Romain Augier, and Vincent Roche. 2021. ^{40}Ar behaviour and exhumation dynamics in a subduction channel from multi-scale ^{40}Ar/^{39}Ar systematics in phengite. Geochimica et Cosmochimica Acta. 311, 141-73.

Leloup, P. H., Mahéo, G., Arnaud, N., Kali, E., Boutonnet, E., Liu, D., and Haibing, Li. 2010. The South Tibet detachment shear zone in the Dinggye area: Time constraints on extrusion models of the Himalayas. Earth and Planetary Science Letters, 292(1-2), 1-16.

Leloup, P. H., Liu, X., Mahéo, G., Paquette, J. L., Arnaud, N., Aubray, A., and Liu, X. 2015. New constraints on the timing of partial melting and deformation along the Nyalam section (central Himalaya): implications for extrusion models. Geological Society, London, Special Publications. 412(1), 131-175.

Li, Haibing, Xu, Z., Niu, Y., Kong, G., Huang, Y., Wang, H., and Liu, D. 2014. Structural and physical property characterization in the Wenchuan earthquake Fault Scientific Drilling project—hole 1 (WFSD-1). Tectonophysics. 619, 86-100.

Li, Yong, Rongjun, Z, AL, D, and MA, E. 2006. Geomorphic evidence for the late Cenozoic strike-slipping and thrusting in Longmen Mountain at the eastern margin of the Tibetan Plateau. Quaternary Sciences. 26(1), 40-51.

Li, H., Su, W., Wang, C. Y., and Huang, Z. 2009. Ambient noise Rayleigh wave tomography in western Sichuan and eastern Tibet. *Earth and Planetary Science Letters*, *282*(1-4), 201-211.

Li, Y., Jia, D., Shaw, J. H., Hubbard, J., Lin, A., Wang, M., and Wu, L. 2010. Structural interpretation of the coseismic faults of the Wenchuan earthquake: Three-dimensional modeling of the Longmen Shan fold-and-thrust belt. *Journal of Geophysical Research: Solid Earth*, *115*(B4).

Li, Z., Kamp, P. J., Liu, S., Xu, G., Tong, K., Danišík, M., and Wu, W. 2023. Late Cretaceous–Cenozoic thermal structure and exhumation of the Eastern Tibetan Plateau margin and its orogenic wedge. *Earth-Science Reviews*, 104319.

Liu, Qi Yuan, Robert D. van der Hilst, Yu Li, Hua Jian Yao, Jiu Hui Chen, Biao Guo, Shao Hua Qi, Jun Wang, Hui Huang, and Shun Cheng Li. 2014. Eastward expansion of the Tibetan Plateau by crustal flow and strain partitioning across faults. Nature Geoscience. 7: 361-65

Lu, R., He, D., Xu, X., and Liu, B. 2016. Crustal-scale tectonic wedging in the central Longmen Shan: Constraints on the uplift mechanism in the southeastern margin of the Tibetan Plateau. *Journal of Asian Earth Sciences*, *117*, 73-81.

Mattauer, M., 1992. The Songpan Garze Triassic belt of west Sichuan and eastern Tibet: a decollement fold belt on a passive margin. Tectonics. 3, 619-26.

Mottram, C. M., D. A. Kellett, T. Barresi, H. Zwingmann, M. Friend, A. Todd, and J. B. Percival. 2020. Syncing fault rock clocks: Direct comparison of U-Pb carbonate and K-Ar illite fault dating methods. Geology. 48, 1179-83.

Nelson, K Douglas, Wenjin Zhao, LD Brown, J Kuo, Jinkai Che, Xianwen Liu, SL Klemperer, Y Makovsky, RJJM Meissner, and James Mechie. 1996. Partially molten middle crust beneath southern Tibet: Synthesis of project INDEPTH results. Science. 274, 1684-88.

Nteme, J., Scaillet, S., Brault, P., and Tassan-Got, L. 2022. Atomistic simulations of ^{40}Ar diffusion in muscovite. Geochimica et Cosmochimica Acta, 331, 123-142.

Nteme, J., Scaillet, S., Gardés, E., Duval, F., Nabelek, P., and Mottolese, A. 2023. Defect-controlled Ar40 diffusion-domain structure of white micas from high-

resolution Ar^{40}/Ar^{39} crystal-mapping in slowly-cooled muscovite. Geochimica et Cosmochimica Acta, 342, 84-107.

Pitard, P., Replumaz, A., Chevalier, M. L., Leloup, P. H., Bai, M., Doin, M. P., and Li, H. 2021. Exhumation history along the Muli thrust—Implication for crustal thickening mechanism in eastern Tibet. *Geophysical Research Letters*, *48*(14), e2021GL093677.

Robert, A., Zhu, J., Vergne, J., Cattin, R., Chan, L. S., Wittlinger, G.and Zhu, L. D. 2010. Crustal structures in the area of the 2008 Sichuan earthquake from seismologic and gravimetric data. Tectonophysics. 491(1-4), 205-210.

Royden, L. H., Burchfiel, B. C., King, R. W., Wang, E., Chen, Z., Shen, F., and Liu, Y. 1997. Surface deformation and lower crustal flow in eastern Tibet. Science: 276 (5313), 788-790.

Royden, L. H., B. C. Burchfiel, and R. D. van der Hilst. 2008. The geological evolution of the Tibetan Plateau. Science. 321, 1054-6.

SBGMR. 1991. Sichuan Bureau of Geology and Mineral Resources, Regional Geology of Sichuan Province. Beijing: Geology House.

Searle, M. P. and A. G. Szulc. 2005. Channel flow and ductile extrusion of the high Himalayan slab-the Kangchenjunga–Darjeeling profile, Sikkim Himalaya. *Journal of Asian Earth Sciences*, *25*(1), 173-185.

Shen, Xiaoming, Yuntao Tian, Guihong Zhang, Shimin Zhang, Andrew Carter, Barry Kohn, Pieter Vermeesch, Rui Liu, and Wei Li. 2019. Late Miocene Hinterland Crustal Shortening in the Longmen Shan Thrust Belt, the Eastern Margin of the Tibetan Plateau. Journal of Geophysical Research: Solid Earth. 124, 11972-91.

Sibson, Richard H. 1992. Earthquake faulting, induced fluid flow, and fault-hosted gold-quartz mineralization. in, Basement Tectonics.

Stöckhert, Bernhard, Manfred R Brix, Reiner Kleinschrodt, Anthony J Hurford, and Richard Wirth. 1999. Thermochronometry and microstructures of quartz—a comparison with experimental flow laws and predictions on the temperature of the brittle–plastic transition. Journal of Structural Geology. 21, 351-69.

Tapponnier, Paul, Xu Zhiqin, Françoise Roger, Bertrand Meyer, and Nicolas Arnaud. 2001. Oblique Stepwise Rise and Growth of the Tibet Plateau. Science. 294, 1671-77.

Tian, Y., Kohn, B. P., Gleadow, A. J., and Hu, S. 2013. Constructing the Longmen Shan eastern Tibetan Plateau margin: Insights from low-temperature thermochronology.*Tectonics*,*32*(3), 576-592.

Tian, Yuntao, Barry P. Kohn, David Phillips, Shengbiao Hu, Andrew J. W. Gleadow, and Andrew Carter. 2016. Late Cretaceous-earliest Paleogene deformation in the Longmen Shan fold-and-thrust belt, eastern Tibetan Plateau margin: Pre-Cenozoic thickened crust? Tectonics. 35, 2293-312.

Vrolijk, Peter, David Pevear, Michael Covey, and Allan LaRiviere. 2018. Fault gouge dating: history and evolution. Clay Minerals. 53, 305-24.

Wang, E., E. Kirby, K. P. Furlong, M. van Soest, G. Xu, X. Shi, P. J. J. Kamp, and K. V. Hodges. 2012. Two-phase growth of high topography in eastern Tibet during the Cenozoic. Nature Geoscience. 5, 640-45.

Wang, E., Meng, K., Su, Z., Meng, Q., Chu, J. J., Chen, Z., and Liang, X. 2014. Block rotation: Tectonic response of the Sichuan basin to the southeastward growth of the Tibetan Plateau along the Xianshuihe-Xiaojiang fault. Tectonics. 33(5), 686-718.

Worley, Brenton A, and Christopher JL Wilson. 1996. Deformation partitioning and foliation reactivation during transpressional orogenesis, an example from the Central Longmen Shan, China. Journal of Structural Geology. 18, 395-411.

Wu, C., Li, H., Leloup, P. H., Yu, C., Si, J., Liu, D., and Gong, Z. 2014. High-angle fault responsible for the surface ruptures along the northern segment of the Wenchuan Earthquake Fault Zone: Evidence from the latest seismic reflection profiles. *Tectonophysics*, *619*, 159-170.

Xu, Xiwei, Xueze Wen, Guihua Yu, Guihua Chen, Yann Klinger, Judith Hubbard, and John Shaw. 2009. Coseismic reverse-and oblique-slip surface faulting generated by the 2008 Mw 7.9 Wenchuan earthquake, China. Geology. 37, 515-18.

Xu, Zhiqin , Shaocheng Ji, Haibing Li, Liwei Hou, Xiaofang Fu, and Zhihui Cai. 2008. Uplift of the Longmen Shan range and the Wenchuan earthquake. Episodes. 31.

Xue, Zhenhua, Wei Lin, Yang Chu, Michel Faure, Yan Chen, Wenbin Ji, and Huaning Qiu. 2021. An intracontinental orogen exhumed by basement-slice imbrication in the Longmenshan Thrust Belt of the Eastern Tibetan Plateau. GSA Bulletin.

Yao, Huajian, Robert D. van der Hilst, and Maarten V. de Hoop. 2006. Surface-wave array tomography in SE Tibet from ambient seismic noise and two-station analysis - I. Phase velocity maps. Geophysical Journal International. 166, 732-44.

Yao, Huajian., Beghein, C. and Van Der Hilst, R. D. 2008. Surface wave array tomography in SE Tibet from ambient seismic noise and two-station analysis-II. Crustal and upper-mantle structure. Geophysical Journal International. 173(1), 205-219.

Yan, Danping, Zhou, M. F., Li, S. B., and Wei, G. Q. 2011. Structural and geochronological constraints on the Mesozoic-Cenozoic tectonic evolution of the Longmen Shan thrust belt, eastern Tibetan Plateau. Tectonics. 30(6).

Yin, An, and T Mark Harrison. 2000. Geologic evolution of the Himalayan-Tibetan orogen. 28, 211-80.

Zhao, G., M. J. Unsworth, Y. Zhan, L. Wang, X. Chen, A. G. Jones, J. Tang, Q. Xiao, J. Wang, J. Cai, T. Li, Y. Wang, and J. Zhang. 2012. Crustal structure and rheology of the Longmenshan and Wenchuan Mw 7.9 earthquake epicentral area from magnetotelluric data. Geology. 40: 1139-42.

Zhang, PeiZhen, Zhengkang Shen, Min Wang, Weijun Gan, Roland Bürgmann, Peter Molnar, Qi Wang, Zhijun Niu, Jianzhong Sun, Jianchun Wu, Sun Hanrong, and You Xinzhao. 2004. Continuous deformation of the Tibetan Plateau from global positioning system data. Geology. 32.

Zhang, Pei-Zhen. 2013. A review on active tectonics and deep crustal processes of the Western Sichuan region, eastern margin of the Tibetan Plateau. Tectonophysics. 584: 7-22

Zheng, Yong, Ping Kong, and Bihong Fu. 2014. Time constraints on the emplacement of klippen in the Longmen Shan thrust belt and tectonic implications. Tectonophysics. 634, 44-54.

Zheng, Yong, Haibing Li, Junjie Li, Guohe Zhang and Jialiang Si. 2022. A comparison study of synkinematic illite isolation, quantitative X-ray powder diffraction, and K-Ar dating for direct fault gouge analyses. Acta Geologica Sinica. Doi: 10.1111/1755-6724.15001.

Zhou, Rongjun, Li Yong, Densmore A. L, Ellis M A, He Yulin, Wang Fenglin, and Li Xiaogang. 2006. Active tectonics of the eastern margin of the Tibet Plateau. Journal of Mineralogy and Petrology. 26(2), 40-51.

Zhu Chengyu, Leloup Philippe Hervé, Wang Guocan, Kai, Cao, Mahéo Gweltaz, Bernet Matthias, WangAn, ShenTianyi, Zhang Pan, Chen Yue, and Wu Guilin. Submitted. Episodic exhumation in the hanging wall of the Muli-Jinpingshan thrust system: Implications on the Cenozoic evolution of SE Tibet. Journal of Geophysical Research Solid Earth.

Supplementary material

S1 River network evolution around the Wenchuan-Maoxian (WM) fault

S2 Results Illite dating MW19-79A and MW19-79E

S3 Analytical procedure for $^{40}Ar/^{39}Ar$ dating

S4 Sample MW19-38A in situ $^{40}Ar/^{39}Ar$ data

S5 Sample MW19-38A step heating $^{40}Ar/^{39}Ar$ data

S6 Sample MW19-10B in situ $^{40}Ar/^{39}Ar$ data

S7 Sample MW19-10B step heating $^{40}Ar/^{39}Ar$ data

S8 Microprobe analytical procedure and X map tool

S9 Microprobe results of MW19-38A and EMPA location

S10 Microprobe results of MW19-10B and EMPA location

S11 Temperature estimate MW19-38A and MW19-10B

Author contributions：

Chenglong GE
Investigation, Data curation, formal analysis, resources, writing- Original Draft, writing - Review & Editing
Philippe Hervé Leloup
Conceptualization, investigation, methodology, supervision, resources, writing – review & Editing,
Yong Zheng
Methodology, formal analysis
Stéphane Scaillet
Data curation, methodology, formal analysis, writing – Review & Editing
Laura Airaghi
Methodology, conceptualization, formal analysis, data curation, writing – Review & Editing
Jinjiang Zhang
Project administration, conceptualization
Florian Duval
Methodology
Haibing Li
Conceptualization, writing - Review & Editing, project administration, funding acquisition

Declaration of interests

☒ The authors declare that they have no known competing financial interests or personal relationships that could have appeared to influence the work reported in this paper.

☐The authors declare the following financial interests/personal relationships which may be considered as potential competing interests:

Highlights:

- First account of three Cenozoic tectonic phases along the Wenchuan - Maoxian fault.
- Direct deformation dating results coherent with thermochronology.
- No pure normal motion on the fault in Cenozoic, no normal component since 25 Ma.
- Fault Kinematics dismiss the crustal channel-flow extrusion model in Longmen Shan.